Journal of Medical Imaging

MedicalImaging.SPIEDigitalLibrary.org

Parameter estimation of atherosclerotic tissue optical properties from three-dimensional intravascular optical coherence tomography

Madhusudhana Gargesha
Ronny Shalev
David Prabhu
Kentaro Tanaka
Andrew M. Rollins
Marco Costa
Hiram G. Bezerra
David L. Wilson

SPIE.

Parameter estimation of atherosclerotic tissue optical properties from three-dimensional intravascular optical coherence tomography

Madhusudhana Gargesha,[a] Ronny Shalev,[b] David Prabhu,[a] Kentaro Tanaka,[c] Andrew M. Rollins,[a] Marco Costa,[c] Hiram G. Bezerra,[c] and David L. Wilson[a,d,*]

[a]Case Western Reserve University, Department of Biomedical Engineering, 10900 Euclid Avenue, Cleveland, Ohio 44106, United States
[b]Case Western Reserve University, Department of Electrical Engineering and Computer Science, 10900 Euclid Avenue, Cleveland, Ohio 44106, United States
[c]University Hospitals Case Medical Center, Harrington Heart and Vascular Institute, Cardiovascular Imaging Core Laboratory, 11100 Euclid Avenue, Cleveland, Ohio 44106, United States
[d]Case Western Reserve University, Department of Radiology, 11100 Euclid Avenue, Cleveland, Ohio 44106, United States

Abstract. We developed robust, three-dimensional methods, as opposed to traditional A-line analysis, for estimating the optical properties of calcified, fibrotic, and lipid atherosclerotic plaques from *in vivo* coronary artery intravascular optical coherence tomography clinical pullbacks. We estimated attenuation μ_t and backscattered intensity I_0 from small volumes of interest annotated by experts in 35 pullbacks. Some results were as follows: noise reduction filtering was desirable, parallel line (PL) methods outperformed individual line methods, root mean square error was the best goodness-of-fit, and α-trimmed PL (α-T-PL) was the best overall method. Estimates of μ_t were calcified (3.84 ± 0.95 mm^{-1}), fibrotic (2.15 ± 1.08 mm^{-1}), and lipid (9.99 ± 2.37 mm^{-1}), similar to those in the literature, and tissue classification from optical properties alone was promising. © *The Authors. Published by SPIE under a Creative Commons Attribution 3.0 Unported License. Distribution or reproduction of this work in whole or in part requires full attribution of the original publication, including its DOI.* [DOI: 10.1117/1.JMI.2.1.016001]

Keywords: optical coherence tomography; image analysis; computational imaging.

Paper 14125R received Sep. 18, 2014; accepted for publication Nov. 25, 2014; published online Jan. 2, 2015.

1 Introduction

Intravascular optical coherence tomography (IVOCT) provides unique high-contrast microscopic resolution imaging of the vasculature.[1–12] With regard to atherosclerotic plaques, IVOCT has demonstrated an ability to differentiate lipid, calcium, and fibrous tissue[13,14] and to quantify microscopic features such as macrophage content.[9] We have previously reported on IVOCT image analysis relating to segmentation, quantification, and visualization of plaques, stents, and other vessel wall components.[15–24] We and others are using IVOCT to assess viability of new coronary artery stent designs[18–25] and quantitative evaluation of atherosclerotic plaques.[15–17] The goal is automated classification and segmentation of plaque types from clinical IVOCT pullbacks. In this report, we focus on computational methods and optimize processing for the reliable determination of tissue optical properties from clinical data.

Trained cardiologists and image analysts can identify tissue types (calcified, lipid, and fibrous tissues) with some accuracy and repeatability, as shown in preclinical and clinical studies.[4,6,12–14] Many use rules established by Yabushita et al.[13] to manually classify tissues. However, modern OCT systems can create over 500 image frames in a single 2.5-s pullback scan, making manual image analysis for research very labor intensive, typically precluding measurements from every image frame. During a demanding clinical procedure, it would be even more difficult to manually analyze hundreds of image frames in clinical decision making. Although IVOCT image quality is outstanding, its limited depth penetration can sometimes confound plaque characterization,[6,25–27] posing challenges for manual analysis, especially in the case of lipid or calcified plaques underlying a fibrous cap. Image quality is affected by any residual blood, but this is not a major concern with current IVOCT blood clearing strategies. Additionally, catheter eccentricity during IVOCT image acquisition may alter the appearance of various plaque features and confuse IVOCT image analysts.[28] To be successful, an automatic computer classification algorithm will need to use all image information available to the human such as intensity, intensity changes, texture, border sharpness, three-dimensional (3-D) shape characteristics, and, perhaps most importantly, physical optical properties.

Several groups have measured tissue optical properties from OCT images in vascular and other tissues using a variety of experimental and theoretical methods. Most use a single-scattering model. We will review reports that measured attenuation and backscattering coefficients in vascular tissues first.[29–33] Xu et al.[29] used a noncatheter-based approach by imaging transverse, fixed tissue sections of coronary arteries; averaged 400 A-lines over time; applied a single-scattering light model; and performed least squares fitting of log transformed, average A-lines to a linear equation. It was concluded that the calcified and fibrotic plaques had a much lower optical attenuation coefficient, μ_t, than lipid plaques, and that lipid and fibrotic plaques had a much higher backscattering coefficient, μ_b, than calcified plaques (lipid: $\mu_b = 28.1 \pm 8.9$ mm^{-1}, $\mu_t = 13.7 \pm 4.5$ mm^{-1}, calcified: $\mu_b = 4.9 \pm 1.5$ mm^{-1}, $\mu_t = 5.7 \pm 1.4$ mm^{-1}, and fibrotic: $\mu_b = 18.4 \pm 6.4$ mm^{-1}, $\mu_t = 6.4 \pm 1.2$ mm^{-1}). Using a catheter-based system and a stationary acquisition without pullback, van Soest et al.[30] measured μ_t in both *in vivo* and

*Address all correspondence to: David L. Wilson, E-mail: david.wilson@case.edu

ex vivo specimens. They corrected for the nonideal imaging system; averaged 15 to 20 A-lines in time; fitted a linear model to log transformed data; and applied an elegant algorithm to determine regions in one dimension corresponding to a single, homogenous tissue type. van Soest et al. argued that μ_b cannot be estimated accurately along with μ_t using a single magnitude OCT value alone at each point and reported only μ_t for calcified (2 to 5 mm^{-1}), fibrotic (2 to 5 mm^{-1}), and lipid (>10 mm^{-1}), yielding trends similar to values reported by Xu et al.[29] Levitz et al.[31] applied a multiple scattering model to OCT images of phantoms and *ex vivo* aortas and estimated scattering coefficients and anisotropy factors. In other studies, OCT data from both phantoms and *ex vivo* arterial samples were fit to single and multiple scattering models.[32,33] Since temporal averaging of frames from a stationary acquisition is undesirable in the clinical setting, frequency domain multiplexing with improvement as compared with simple linear filtering has been proposed to reduce speckle in single A-lines for optical property measurement.[34] As reviewed in Sec. 5, there is variability in reported μ_t values between research groups due to methodological differences including parameter estimation approaches.

Optical properties have also been estimated in other tissues using OCT. Yang et al.[35] determined the optical scattering coefficient, μ_s, from unfixed normal and malignant, *ex vivo* ovarian tissues. They found that the absorption coefficient, μ_a, for ovarian tissue is small (~0.006 mm^{-1}) and that μ_t was a good approximation to μ_s. Knu et al.[26] determined the optical parameters from OCT images of pig and human skin using a multiple scattering model. Lee et al.[36] have studied the performance of single and multiple scattering models using *in vitro* rat livers and *in vivo* human skin. The methodologies were similar to those used in blood vessels with 100 to 200 A-lines averaged prior to fitting. In general, it is evident from the literature that a single-scattering model is reasonable and is probably the only statistically appropriate solution for noisy clinical IVOCT images.

A goal is to fully automate tissue characterization in 3-D IVOCT clinical pullbacks. Some recent reports use machine learning for plaque classification from both preclinical and clinical IVOCT data.[37,38] Ughi et al.[38] used μ_t estimates from a layer model applied to single A-lines and two-dimensional (2-D) texture and geometric measures as features for classification. Athanasiou et al.[37] used 2-D texture and intensity features alone and assumed "islands" of calcified tissue surrounded by other tissue types, which is not necessarily true in many image frames. These reports are encouraging and show that improved 3-D estimation of optical properties could improve the classification.

The rationale for our research plan is as follows. Although it is clear that the optical properties of plaques, such as the attenuation coefficients, will be useful discriminatory features for automated tissue classification, extracting optical properties from clinical IVOCT data remains a challenge. Stationary acquisitions[29,30] are untenable, as they will require an additional blood clearing operation to sample a single location. Estimation from single, noisy A-lines gives large estimation variance. Hence, our solution is to estimate optical properties from small 3-D volumes of pullback image data and to use advanced parameter estimation approaches which are robust against noise outliers. In addition, we use *in vivo* clinical data rather than image data from *ex vivo* samples as is typically used. This avoids typical limitations of *ex vivo* imaging including potential tissue degradation, no mean and/or pulsating pressure, no cardiac motion, unrealistic temperatures, no blood artifacts, and a straight path pullback rather than actual 3-D coronary geometry. Moreover, in the event of spatially inaccurate, sparse histological sampling, one can make inappropriate "ground truth" determinations using *ex vivo* data. Instead we use ground truth volumes of interest (VOIs) identified by trained analysts using well-established criteria. Although independent histological verification is desirable, there is no way to obtain it on *in vivo* clinical data. Moreover, our approach is quite appropriate for optimizing the 3-D parameter estimation methods in this report. Methods should be equally applicable to 3-D cancer imaging.

In this report, we correct the nonideal characteristic of OCT imaging systems, use noise reduction filtering, estimate optical parameters from small VOIs rather than single A-lines, reject outliers, identify goodness-of-fit measures suitable for determining the quality of optical property estimates, and determine how well optical properties alone can be used to classify plaque types. Our basic paradigm is to compare estimation results across 311 manually annotated VOIs.

2 Experimental Methods and Catheter Correction

Images used in this study were selected from the database available at the Cardiovascular Imaging Core Laboratory of the University Hospitals Case Medical Center (Cleveland, Ohio), called the Core Lab. These images were collected on the C7-XR swept-source OCT system (St. Jude Medical Inc., Westford, Massachusetts). It has a swept laser source with a 1310-nm center wavelength, 110-nm wavelength range, 50-kHz sweep rate, 20-mW output power, and ~12-mm coherence length. The pullback speed was 20 mm/s and the pullback length was 54 mm. A typical pullback consisted of 271 image frames spaced ~200 μm apart. The test dataset consisted of 35 IVOCT pullbacks of the left anterior descending and the left circumflex coronary arteries and was chosen to be representative of typical OCT scans obtained from patients prior to stent implantation.

To more accurately estimate μ_t, we need to account for certain characteristics of the IVOCT imaging system. We used methods similar to those of van Soest et al.[30] The imaging system response in the presence of tissue attenuation μ_t is given below:[30]

$$I(r) = I_0 T(r) S(r) \exp(-\mu_t r) + I_{off}, \tag{1}$$

with

$$T(r) = \left[\left(\frac{r - z_0}{z_R}\right)^2 + 1\right]^{-1/2}, \tag{2}$$

$$S(r) = \exp\left[-\left(\frac{r - z_C}{z_W}\right)^2\right], \tag{3}$$

where r is the depth, I is the detected intensity, I_0 is the initial intensity, I_{off} is the detected intensity at a depth of $r = 0$, μ_t is the attenuation coefficient, $T(r)$ is the confocal function with z_0, the position of the beam waist and with z_R, the Rayleigh length, and $S(r)$ accounts for the spectral coherence of the source in Fourier-domain OCT with parameters z_W (representing the half-width of the intensity roll off) and z_C (representing the center of the scan).

Intact catheters without a guide wire were inserted into a bottle containing water or low concentration intralipid solution. The catheter was firmly held in place using a vice-grip on the catheter outside the bottle. The water image was used to estimate background intensity. A low concentration 1:128 intralipid (Sigma Aldrich, 20%, emulsion) diluted in water provided an image of scatterers without significant attenuation. Stationary image sequences of 121 image frames and pullback sequences of 271 image frames were obtained. About 100 IVOCT magnitude images were averaged. From the average frame, we averaged 500 A-lines to obtain a very low noise A-line.

In intralipid images, we assumed μ_t to be low, eliminating the tissue attenuation term $[\exp(-\mu_t r)]$. I_{off} was estimated from the water images. z_C and z_W were obtained from the interferometer setting and the specifications of the light source, respectively. With these parameters fixed, I_0, z_0, and z_R were estimated by fitting Eq. (1) to average A-line data using nonlinear least squares with the Nelder–Mead simplex optimization. A-line data were truncated to exclude bright reflection from the catheter sheath. Model fits were compared over pullbacks, catheters, and acquisition modes (stationary versus pullback). Similar fits were obtained in each case with less than 3% variation in parameters. Clinical images were corrected using Eq. (1). We subtracted I_{off}, the baseline intensity, and divided A-line intensities by the term $I_0 \cdot T(r) \cdot S(r)$.

3 Image Analysis

3.1 *Volumes of Interest*

We developed specialized software in MATLAB for obtaining user-defined VOIs and for evaluating their optical properties. In the software, pullbacks were loaded and image frames were presented to the expert, an IVOCT image analyst, in both (x, y) and (r, θ) views. Image data came from a manually analyzed Core Lab study aimed at classifying plaque types and plaque burden prior to stent implantation. The study classified quadrants of IVOCT images as either fibrous, lipid, calcium, or normal. Core Lab analysts were well trained in interpreting OCT image data. For our study, the analyst determined start and stop image frames for a homogeneous VOI. Then, in the (r, θ) view, the analyst segmented the VOI using freehand brush strokes and applied a plaque-type label (fibrous, lipid, or calcified). All segmentations and labels for VOIs were saved in a convenient data structure for easy retrieval and analysis. Standard criteria were used by analysts to identify the various plaque types in pullback image frames.[13] Fibrous plaques were characterized by homogeneous, signal-rich regions; calcified regions by signal-poor regions with sharp borders; and lipid plaques by signal-poor regions with diffuse borders. In this study, we used 311 VOIs from 35 pullbacks. The VOIs were of various sizes and shapes. Most consisted of 2 to 5 image frames, 50 to 200 A-lines, and 20 to 50 sample points in each A-line.

3.2 *Parameter Estimation of Tissue Optical Properties*

Each VOI was processed as follows. We applied 2-D noise reduction filtering to linear data using a variety of filters [average filter (AF), median filter (MF), and Lee speckle reduction filter (LF)[39]] with parameters listed later. To avoid any "edge effects" during filtering, we applied 2-D filtering to entire image frames and subsequently used the stored spatial coordinates of each VOI to extract a "filtered" VOI. Any A-line with fewer than five samples (points) was removed from consideration. Rearranging and taking the natural logarithm of Eq. (1), we get the equation below:

$$\ln\left\{\frac{[I(r) - I_{off}(r)]}{[T(r; z_0, z_R) \cdot S(r)]}\right\} = \ln(I_0) - \mu_t r. \quad (4)$$

In the event that the left-side term within square brackets was ≤ 0, we set its value to $+1$. Equation (4) reduces to fitting a straight line to the data. Parameter estimation methods included individual line (IL) fits and parallel line (PL) fits to A-lines. In IL fitting, a slope and intercept are fit to each A-line in a collection of adjacent A-lines. In PL fitting, we fit one slope and multiple intercepts to the collection as is rationalized next. Assuming locally homogeneous tissue within a VOI, there should be a single characteristic μ_t value and a single slope. Intercepts depend upon distance from the catheter, the angle of incidence with the lumen, depth in tissue, and so on, which are observations consistent with the PL approach. Moreover, a PLs' model has many fewer parameters making it less sensitive to noise. In addition, we have also employed methods that perform statistical analysis to reject data outliers for which we use the term "robust." The methods were:

- *IL, individual A-lines*: Each corrected A-line was fit to Eq. (4) yielding a set of μ_t and I_0 values. Extreme outliers, i.e., lines with negative μ_t, were removed. Means of μ_t and I_0 were reported. Standard errors (SEs) were computed from $\mathrm{SE} = \mathrm{SD}/\sqrt{n}$, where SD is the standard deviation and n is the number of A-lines processed.
- *α-T-IL, individual A-lines with α trimming*: In this robust parameter estimation approach, we determined μ_t and I_0 for each A-line, removed extreme outliers, and rank ordered results. A predetermined percentage, α, of μ_t's (and corresponding I_0's) from the top and bottom of the distribution was removed, and new mean μ_t and I_0 values were obtained. SEs were computed using the same strategy as above.
- *IT-IL, individual A-lines with iterative trimming*: In this robust parameter estimation approach, we determined μ_t and I_0 for each A-line, removed extreme outliers, and computed a new mean μ_t and I_0. We then iteratively removed A-lines with μ_t's outside mean $\pm$ 2 (SD), with empirically determined $n = 3$ iterations. Finally, a mean μ_t and I_0 were computed from the remaining A-lines and reported. SEs were computed as above.
- *PL, Parallel line fit to A-lines*: We determined a μ_t and I_0 for each A-line using IL fits and removed extreme outliers. On the remaining A-lines, a PL model with a single slope and multiple intercepts was estimated, giving a single μ_t and multiple I_0's. SEs were computed from the MATLAB toolbox function *aoctool*.
- *α-T-PL, Parallel lines with α trimming*: In this robust approach, we determined a μ_t and I_0 for each A-line using IL fits, removed extreme outliers, and rank ordered results. A predetermined percentage, α, of μ_t's (and corresponding I_0's) from the top and bottom of the distribution was removed. A PL model was

applied to the remaining A-lines. Parameter uncertainty errors were computed as above.

IT-PL, Parallel lines with iterative trimming: In this robust approach, we determined a μ_t and I_0 for each A-line using IL fits, removed extreme outliers, and computed a new mean μ_t and I_0. We then iteratively removed A-lines with μ_t's outside the mean $\pm 2(\mathrm{SD})$ with an empirically determined $n = 3$ iterations. A PL model was applied to the remaining A-lines. Parameter uncertainty errors were computed as above.

NIL-PL-TM, Individual lines followed by parallel lines followed by noniterative trimming: In this robust approach, we determined a μ_t and I_0 for each A-line using IL fits, removed extreme outliers, and applied a PL fit to obtain a single-slope μ_{PL} and a standard deviation SD_{PL}. Next, we kept only those A-lines with individual μ_t's within $\mu_{PL} \pm 2(\mathrm{SD}_{PL})$. We then computed mean μ_t and I_0 and reported values. SEs were computed using the strategy for IL.

IL-PL-TM, Individual lines followed by parallel lines followed by iterative trimming: In this robust approach, we determined μ_t and I_0 for each A-line and removed extreme outliers. We applied a PL model to obtain a single slope, μ_{PL}, and a standard deviation, SD_{PL}. Next, we kept only those A-lines with individual μ_t's within $\mu_{PL} \pm 2(\mathrm{SD}_{PL})$. We iterated this process (PL fit and removal of A-line outliers) two more times. We computed a mean μ_t and I_0 from the IL fits. SEs were computed using the strategy for IL.

3.3 *Data Analysis*

For each VOI, we obtained μ_t and I_0 estimates for each combination of filtering (three methods) and parameter estimation (eight methods). Goodness-of-fit measures included coefficient of variation (CV) given by the ratio of the parameter uncertainty to the point estimate, the root mean square error (RMSE), and adjusted R^2, calculated as described in Ref. 40. For good filtering and estimation methods, we want: (1) small parameter uncertainty intervals, (2) small spread of point estimates across many VOIs of a particular tissue type, (3) superior goodness-of-fit values (high adjusted R^2, low RMSE, and low CV), and (4) high sensitivity/specificity from parameter estimates using a supervised classifier.

3.4 *Processing Parameters*

We optimized the processing parameters in preliminary experiments. The size of the filter window (7×7) and other parameters was tuned by examining their role on image appearance as well as μ_t estimates. It should be noted that a filter kernel of length 7 is approximately the same size as the 35 μm axial point spread function of our system. We used a 7×7 window for the LF, AF, and MF. Since VOIs were of irregular shape, we obtained some short A-line segments which were omitted if they contained fewer than five samples. To avoid fitting the baseline noise floor, we ended consideration of A-line samples along r when there was a run of nine samples below the baseline value of six in the original linear data. This occurred in less than 1% of A-lines as experts did not mark VOIs at large depths in the tissue. For robust estimation with α trimming, we experimentally determined an optimal value of $\alpha = 10\%$. For iterative estimation methods, we experimentally determined that three iterations and two SDs gave good results. More details about optimization experiments are in Sec. 4.

In an exploratory classification experiment, we used three features (μ_t, $\langle I \rangle$, I_0), and a support vector machine (SVM) classifier with a linear kernel, fivefold cross validation, and feature normalization. We used one-against-all to identify three tissue

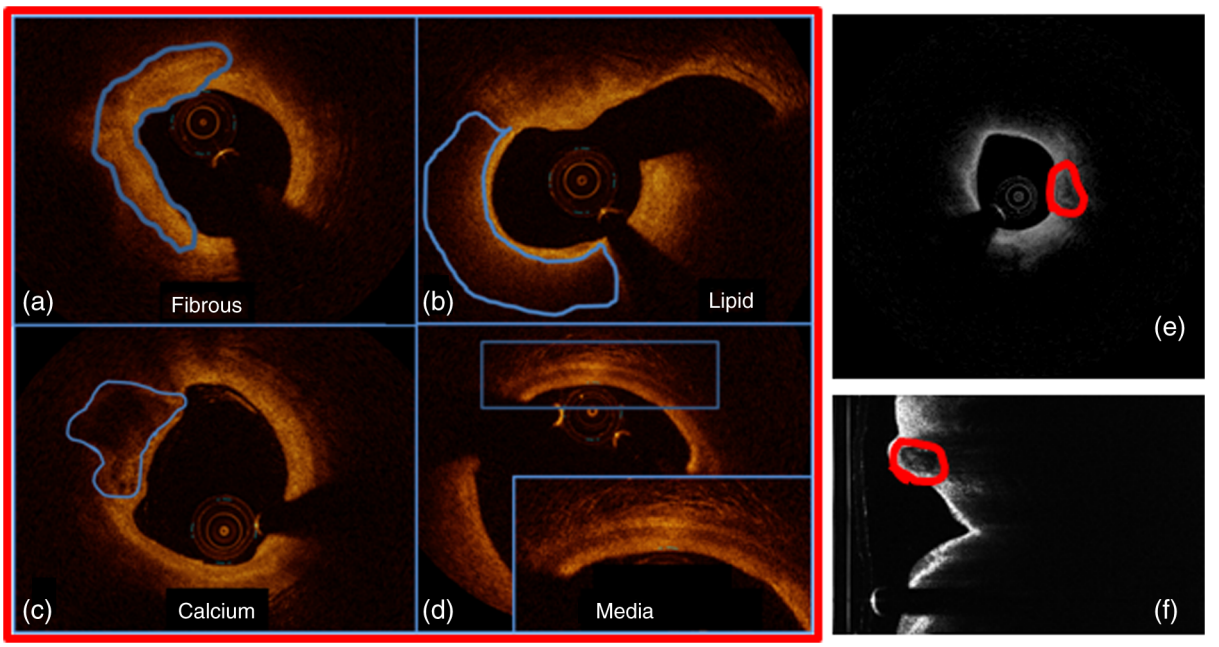

Fig. 1 Appearance of atherosclerotic tissue types in IVOCT images. They are: (a) fibrous, (b) lipid, (c) calcium, and (d) normal (media). The latter includes a zoomed inset to show the typical layered appearance. In (e) and (f), a sample IVOCT image frame is shown in the (x, y) (anatomical) and (r, θ) (polar) views, respectively. A calcified region is identified in red in both frames.

types. Parameter settings of the classifier were determined from preliminary optimization experiments with a subset of VOIs. We weighted samples in inverse proportion to their prevalence.[41] Performance results were averaged across the five folds.

4 Results

Example IVOCT images in Figs. 1(a)–1(d) show calcified, fibrotic, lipid, and normal (media) regions in the (x, y) view. Figures 1(e) and 1(f) show a sample IVOCT image frame from a clinical pullback in both (x, y) (anatomical) and (r, θ) (polar) views, with a calcified region identified in red. The VOIs were marked on (r, θ) view because all subsequent processings were done on (r, θ) image data. The VOIs were mapped to (x, y) for presentation (Fig. 2). We have observed that, in general, the tissue types in a region of interest do not change much across successive frames, i.e., they have a high correlation, justifying the use of volumetric analysis in our study (Fig. 2).

We obtained images of intralipid and water and fitted the data to the system model. Average A-lines from a stationary acquisition are shown in Fig. 3. We ignored the very small upward trend in water and used an average value for I_{off}. Water images were similar across the three tested catheters, and I_{off} values were close to baseline values at large r in clinical images. Using the average A-line from dilute intralipid images, Eq. (1) was fit to data over the "imaging range" from 1 to 2.5 mm. As described previously, values for I_0, z_0, and z_R were estimated using a least squares fit [Fig. 3(b)] and other parameters were obtained from system specifications. Parameters for the typical catheter in Fig. 3 were: $I_0 = 155$, $z_0 = 1.06$ mm, $z_R = 0.59$ mm, $I_{\text{off}} = 6.39$, $z_C = 0$ mm, and $z_W = 12$ mm.

We determined the sensitivity of μ_t estimates to the correction model parameter estimates. Table 1 shows the result for representative VOIs using PLs to estimate μ_t. Values of μ_t changed by only 3% to 7% with and without catheter correction. To study the potential effect of variation between catheters, we perturbed catheter parameters over a $\pm 5\%$ range (a variation much larger than observed) and determined the effect on μ_t. In general, different catheter correction parameters had a relatively minor effect (typically <3%) on μ_t, smaller than the uncertainty due to noise (see Sec. 4). Varying z_0 had a bigger effect than varying z_R.

Preprocessing methods were systematically tuned. Individual A-lines with speckle were quite noisy and were visually evident only after filtering trends. Using IL parameter estimation, noise reduction filters substantially reduced SE uncertainties of μ_t estimates [Fig. 4(a)]. SE was reduced from 0.8442 [no filtering (NF)] to 0.5371 using AF, 0.446 using MF, and 0.1923 using LF. Therefore, LF was deemed the best filtering approach. Small variations in point estimates were obtained, but effects were

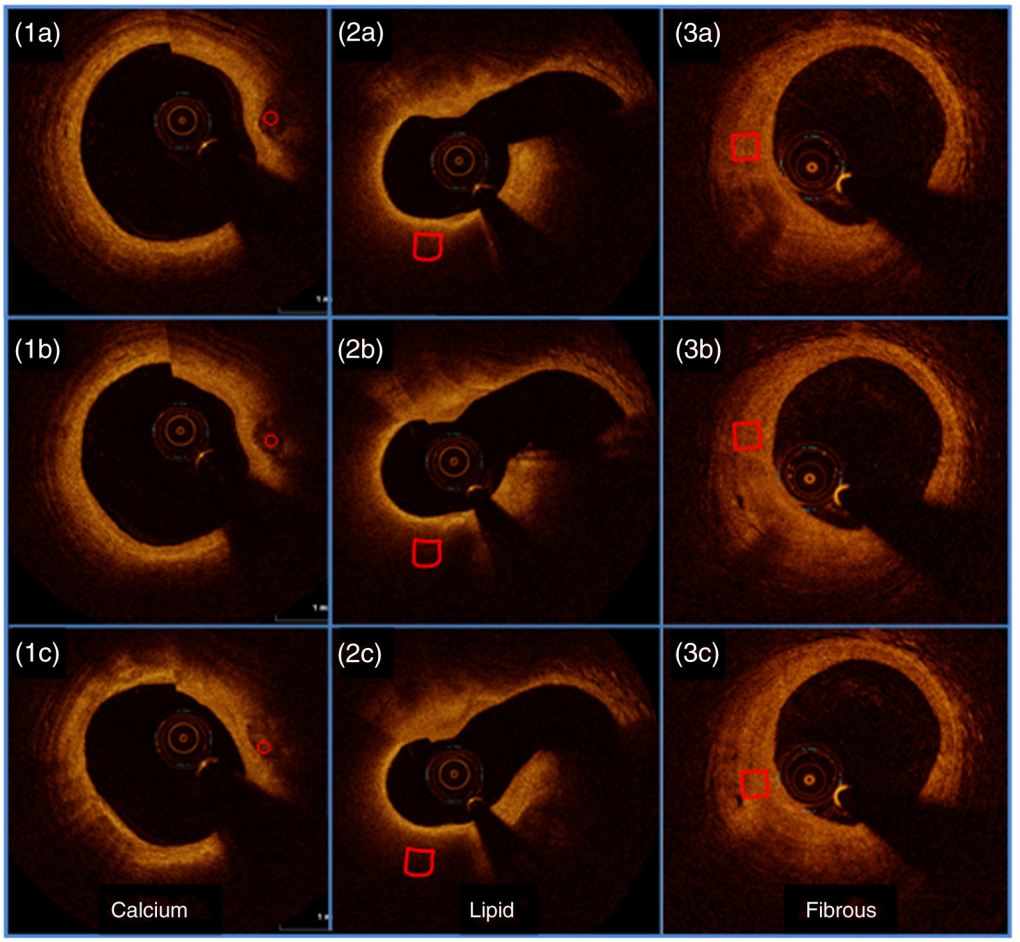

Fig. 2 Marking of VOIs in images across frames. Columns contain three successive image frames for (1a–1c) calcium, (2a–2c) lipid, and (3a–3c) fibrous, corresponding to a single VOI. Because tissue types are preserved across a few image frames with 200 μm spacing, we can process A-lines within VOIs. In practice, such multiple VOIs would be obtained from a single homogenous region (not shown).

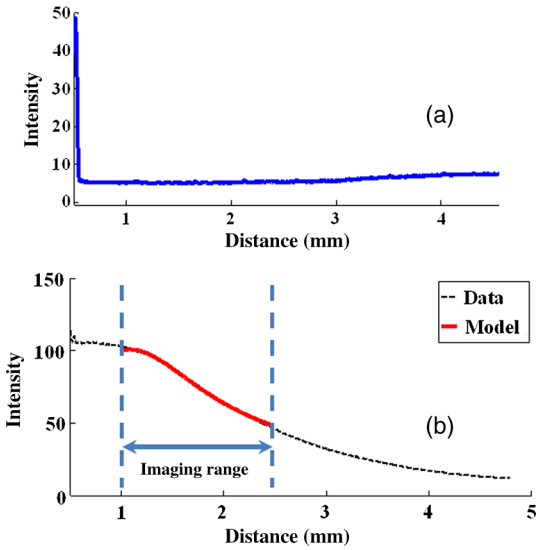

Fig. 3 Determination of imaging system model parameters. The average A-line in water is shown in (a) with intensity on a linear scale. In (b), we plot the average A-line in intralipid (1 : 128 dilution). We fit data within the "imaging range," as shown in red. $z_0 = 1.057$ mm and $z_R = 0.590$ mm were estimated from these data. $z_C = 0$ mm and $z_W = 12$ mm were otherwise obtained. Image data were acquired in stationary mode and about 100 A-lines across time and θ were averaged.

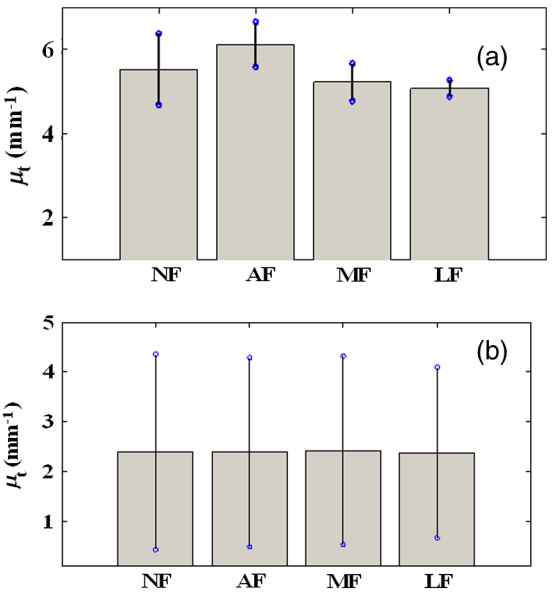

Fig. 4 Effect of filtering on μ_t estimates obtained with IL. In (a), a single calcium VOI with 122 A-lines was analyzed. IL was used to estimate μ_t with no filtering (NF) and the three filtering methods—average filter (AF), median filter (MF), and Lee filter (LF). Small (<5%) changes of point estimates were obtained, but there were inconsistent trends across other VOIs. Standard errors (SEs) were 0.8442 (NF), 0.5371 (AF), 0.446 (MF), and 0.1923 (LF). NF gave the largest uncertainty SE expressed as a percentage of the point estimates (~17%), while LF gave the smallest (4%). (b) 106 calcium VOIs were analyzed using IL and different filter treatments. Means and standard deviations of μ_t are plotted. The LF had the smallest standard deviation across VOIs.

inconsistent across VOIs, reducing the concern of potential bias. Effects of noise reduction were less dramatic when using other parameter estimation approaches, but trends were similar. Since we want estimates to help distinguish one tissue type from another, we analyzed the effect of filtering on the spread of estimates for a single tissue type across many VOIs. For calcium, LF reduced the spread of estimates by about 13% [Fig. 4(b)]. Similar results were obtained across other tissue types.

To optimize α in noniterative trimming, we varied α from 0% to 40% in steps of 5%, and at each step, we computed μ_t and the resulting RMSE for each VOI in a set of 84 VOIs drawn from all three plaque types. Figure 5 shows the average RMSE across VOIs plotted against α. The optimum RMSE was $\alpha = 10\%$, and this was used in subsequent experiments. Similarly, we optimized k in iterative trimming, which preserved A-lines with μ_ts in the range (mean $\pm\, k \cdot$ std). We estimated μ_t and RMSE with $k = 1$, 2, or 3 and obtained an average RMSE versus k curve. The optimal $k = 2$ was used in subsequent experiments (not shown).

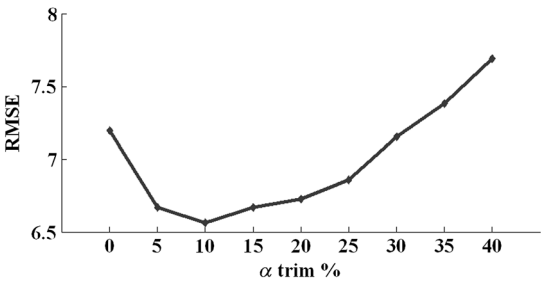

Fig. 5 Determination of optimal α for trimming. Using 84 VOIs drawn from all three plaque types, we obtained RMSE versus α for each VOI. The average RMSE curve plotted gave a minimum at $\alpha = 10\%$.

Table 1 Effect of catheter correction on μ_t estimates obtained with the parallel lines' (PLs') method for a single-representative VOI from each tissue type. The first two columns show μ_t estimates within the VOI with and without catheter correction. Fibrotic shows the least variation (3.8%), while calcium (7.8%) and lipid (7.6%) show a larger variation in μ_t. We also applied a ±5% perturbation to z_0 (around a nominal value) keeping z_R fixed, and repeated the experiment with a ±5% perturbation to z_R (around a nominal value) keeping z_0 fixed. Perturbation had a minor effect (<3% in most cases) on μ_t estimates.

Tissue type	No correction	Correction w / Cath 5	$z_0 = 0.984$ mm −5%/ + 5%	$z_R = 0.628$ mm −5%/ + 5%
Calcium	2.54	2.35	2.34 (0.43%)/2.37 (0.85%)	2.36 (0.43%)/2.35 (0%)
Fibrotic	2.08	2.00	2.06 (3%)/1.91 (4.5%)	2.00 (0%)/1.99 (0.5%)
Lipid	5.50	5.14	5.13 (0.19%)/5.16 (0.39%)	5.16 (0.39%)/5.13 (0.19%)

Note: All numbers in table refer to the μ_t estimate in mm^{-1}.

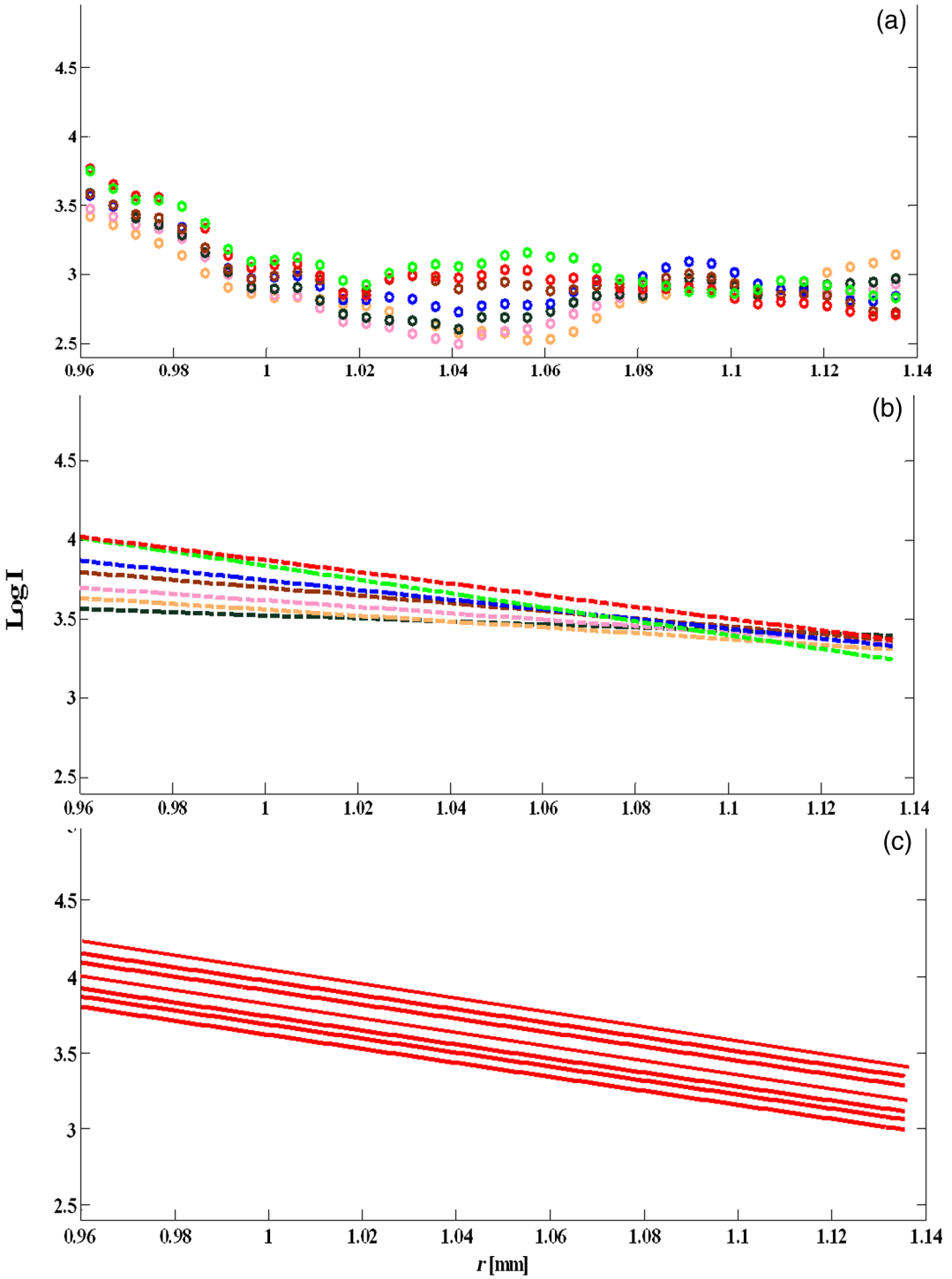

Fig. 6 A subset of seven A-lines from an example calcified VOI (a) is shown. These A-lines are fitted using IL (b) and PL (c). In (a) and (b)s, A-lines have been color coded for clarity. (c) PL fitting where all fitted lines (red) have same slope but different intercepts. The μ_t estimates (mean $\pm$ std. error) were IL (2.59 ± 0.24 mm^{-1}) and PL (2.63 ± 0.14 mm^{-1}). The PL typically results in smaller parameter uncertainty and a more accurate estimate.

We next compared the parameter estimation approaches. Figure 6 illustrates IL and PL. In this calcified VOI, PL gave a reduced parameter uncertainty (which results in a more robust and accurate estimate) as compared with IL (see legend). Using processing parameters from the above paragraph and LF, we examined the effects from the eight parameter estimation approaches. For a typical calcium VOI, α-T-PL and PL gave smaller parameter uncertainty and SEs than other techniques (Fig. 7). There were small changes in point estimates, but across VOIs, there were no obvious trends. Over 111 fibrotic VOIs, the distribution of μ_t as a function of estimation methods is shown in Fig. 8(a) without censoring and Fig. 8(b) with censoring. Censoring was done to remove VOIs having bad fits, i.e., RMSE > 6. With censoring on RMSE, the number of outliers

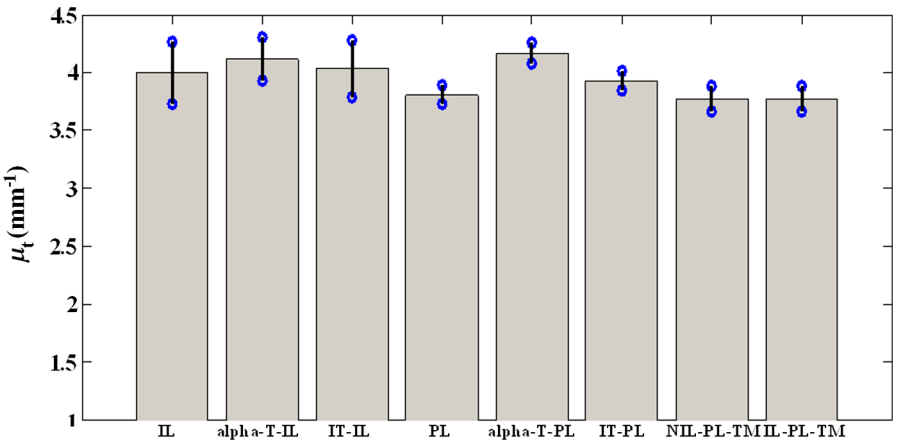

Fig. 7 Comparison of parameter estimation methods. A typical calcium VOI containing 62 A-lines was analyzed following LF. The following results were obtained (mean $\pm$ std. error of μ_t): (1) IL: 3.99 ± 0.27 (8 lines removed), (2) α-T-IL: 4.11 ± 0.18 (24 lines removed), (3) IT-IL: 4.03 ± 0.24 (14 lines removed), (4) PL: 3.81 ± 0.08 (8 lines removed), (5) α-T-PL: 4.17 ± 0.08 (24 lines removed), (6) IT-PL: 3.93 ± 0.09 (14 lines removed), (7) NIL-PL-TM: 3.78 ± 0.11 (38 lines removed), and (8) IL-PL-TM: 3.78 ± 0.11 (39 lines removed). α-T-PL and PL methods gave the smallest estimated uncertainty.

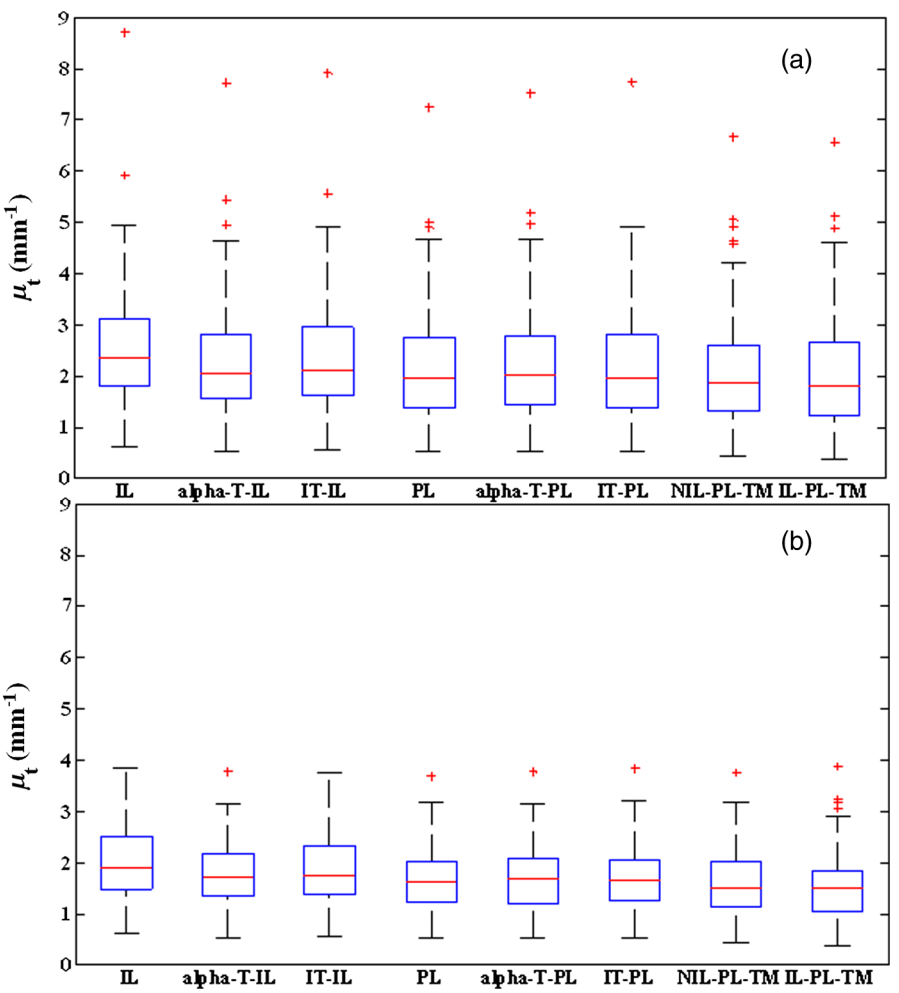

Fig. 8 Box whisker plot of μ_t as a function of estimation methods for (a) 111 fibrotic VOIs, and (b) a censored subset of 79 VOIs obtained by applying an RMSE threshold of 6. The red bar is the median, the edges of box are 25th and 75th percentiles, and the whiskers represent the most extreme points that are not outliers. Outliers are denoted with red +'s. The RMSE censoring greatly reduced the number of very large outliers and spread of μ_t estimates. With censoring, rank ordering on standard deviation across VOIs is α-T-PL < PL < IT-IL < α-T-IL < IL-PL-TM < IT-PL < IL-PL-TM < IL. The (mean $\pm$ std) of μ_t for methods is: IL (2.55 ± 1.16), α-T-IL (2.26 ± 1.10), IT-IL (2.35 ± 1.10), PL (2.14 ± 1.09), α-T-PL (2.18 ± 1.09), IT-PL (2.18 ± 1.11), NIL-PL-TM (2.06 ± 1.10), and IL-PL-TM (2.03 ± 1.13).

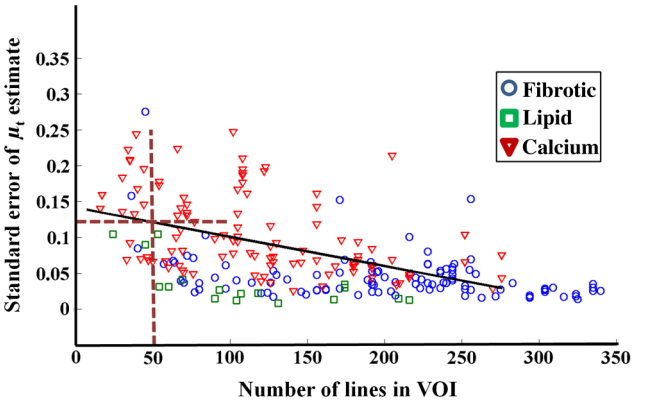

Fig. 9 Effect of number of A-lines on μ_t estimates. SE of μ_t estimates tends to reduce with VOIs having more A-lines. Processing included LF, α-T-PL, no censoring. Tissue types are color coded. The mean number of A-lines was 150 and 80% of homogenous regions have ≥50 A-lines. The solid black line is a linear fit that predicts an uncertainty SE ~ 0.12 mm^{-1} with 50 A-lines.

in μ_t was greatly reduced. Since censoring tended to remove VOIs having very large μ_t estimates, means were reduced with censoring. Also, the error bars were smaller after censoring as compared with before censoring, which meant that the μ_t estimates were more robust after censoring.

Since we are ultimately interested in automated processing, we analyzed the role of the size of the region of support on μ_t estimates. Figure 9 shows a scatter plot of numbers of A-lines in VOIs versus SE of μ_t. In general, lower SEs were obtained for VOIs containing more A-lines. A large percentage (>80%) of VOIs had 50 or more A-lines in them. This suggests that the experts identified many homogeneous regions with >50 A-lines and average length of 35 samples. The VOIs having at least 50 A-lines resulted in an SE of typically <5% of the μ_t estimate.

We are especially interested in goodness-of-fit measures because they could become features in an automated machine learning approach to classify plaque types. Adjusted R^2 (Ref. 40) is a good method for comparing fits of models with different numbers of parameters [Fig. 10(a)]. Methods α-T-PL, PL, and IT-PL had higher adjusted R^2 than other methods, indicating the appropriateness of PLs, a general observation across VOIs. We observed improvements with PLs because the number of free parameters was reduced from $2M$ to $M+1$, where M was the number of A-lines. Although the adjusted R^2 is a good method to compare model order, its dependence on slope does not allow comparisons across VOIs. For fibrous VOIs, RMSE and CV histograms were plotted [Figs. 10(b) and 10(c)].

More than 90% of VOIs had RMSE < 12. The RMSE was deemed the most appropriate goodness-of-fit for censoring VOIs. When VOIs with large RMSEs were omitted, the variability of μ_t estimates was reduced (Fig. 8) and classification (Table 3) improved.

To evaluate the usefulness of optical properties as features in an automatic classifier for atherosclerotic plaque tissue types, we used three features (μ_t, $\langle I \rangle$, I_0), where $\langle I \rangle$ was the mean intensity in the VOI. Intensity features are related to the backscattering characteristics of the tissue within the VOI as well as any attenuation prior to the VOI, features which should aid prediction of class membership. We used supervised classification, SVM,[41] fivefold cross validation, and one against all for each of the three classes (Table 3). Data were processed without and with RMSE-based censoring, where VOIs with RMSE > 12 were excluded. Classification improved with censoring [compare Tables 3(a) and 3(b)]. (The RMSE threshold is different from that used in Fig. 8 because we wanted to be uniform across all three tissue classes.) Figure 11(a) shows a clear separation of classes in 3-D feature space following VOI censoring. Features (μ_t, $\langle I \rangle$), the two best features, also demonstrated good separation in Fig. 11(b).

With all analyses considered, we determined that the PLs and α trimming were both useful, with PL and α-T-PL producing numerically close μ_t estimates. In general, we recommend α-T-PL, LF, and possible censoring on RMSE value as best choices. Using these choices, we obtained the following values of μ_t: calcified (3.84 ± 0.95 mm^{-1}), fibrotic (2.15 ± 1.08 mm^{-1}), and lipid (9.99 ± 2.37 mm^{-1}). Computational estimation of μ_t allowed us to distinguish between lipid plaques and calcium

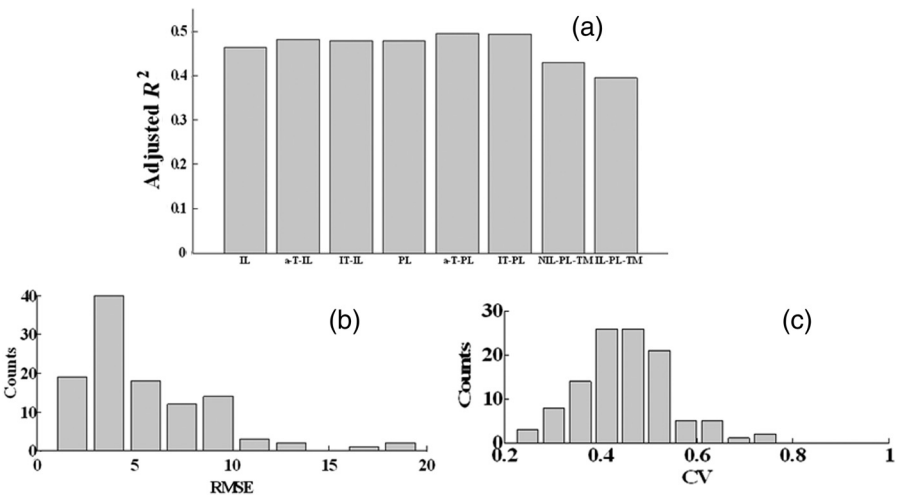

Fig. 10 Goodness-of-fit measures. (a) Adjusted R^2 is plotted as a function of parameter estimation method for a single-fibrotic VOI with 240 A-lines. The PL, α-T-PL, and IT-PL gave higher adjusted R^2 than others. (b) Histogram of RMSE for 111 fibrotic VOIs for α-T-PL. More than 90% had good fits with RMSE < 12. (c) Using the same data, over 85% of VOIs have a CV < 0.5.

Table 2 Estimates of μ_t are consistent with values from two previously reported studies[29,30] that have estimated optical properties of atherosclerotic plaques using the same imaging system (1310-nm center wavelength and 110-nm wavelength range).

Tissue type	μ_t (estimated) (mm^{-1})	μ_t (literature) (mm^{-1})
Calcified	3.84 ± 0.95	2–5
Fibrotic	$2.15 + 1.08$	2–5
Lipid	9.99 ± 2.37	≥10

plaques with a diffuse edge (Fig. 12). Typically, this is resolved by experts only after analyzing adjacent frames.

5 Discussion

The characterization of tissue optical properties from 3-D IVOCT clinical pullbacks will be an important step in reliable tissue classification. Previous methods for estimating optical properties have typically used time-averaged data in a stationary acquisition[29] or single A-lines from a pullback.[30] Since stationary acquisitions are clinically impractical and single A-lines are extremely noisy, we created a 3-D approach whereby groups of A-lines close to each other are analyzed together. Innovations in this report include: use of A-lines from within a 3-D VOI to improve stability of estimates; advanced, robust parameter estimation approaches including goodness-of-fit estimates; and a rigorous methodology for comparing estimation methods applied to clinical pullback data. Results suggest that filtering is desirable, that estimates vary some with the method used, that PL and its variants generally outperformed IL and its variants, and that RMSE is the favored goodness-of-fit measure which can be used effectively to "censor" VOIs with bad fits. As detailed later, we deemed α-T-PL as best. In general, we can conclude that the PL model, which fits one slope and multiple intercepts to a collection of spatially adjacent A-lines, is appropriate since there should be a single characteristic μ_t value and a single slope for locally homogeneous tissue.

LF[39] was the best filtering method among those tested. Filtering visually reduced the noise in A-lines. Comparing filters on a single VOI, the uncertainty of μ_t was minimized with the LF [Fig. 4(a)]. Also, LF reduced the spread of μ_t across many VOIs for a given tissue [Fig. 4(b)], presumably enabling better separation of tissues. We did not observe any consistent bias due to filtering on μ_t estimates. It is satisfying that a filter designed for speckle noise gave the best results for parameter estimation because speckle is the dominant noise in OCT images.

Comparing parameter estimation methods via multiple assessments, we determined that PLs and α trimming were useful and that the best overall method was α-T-PL. Comparing results on a typical VOI, the uncertainty of μ_t was least for α-T-PL (Fig. 7). Since we are ultimately interested in separating tissue types, reducing the spread of μ_t estimates across many VOIs is desirable. α-T-PL and PL gave a reduced spread of μ_t across many VOIs as compared with other methods (Fig. 8, legend). Since results were variable across filters, VOIs, tissue types, and estimation methods, we developed a voting scheme for comparing parameter estimation methods. For each VOI, we picked a winning technique based on two different criteria: (1) the smallest uncertainty SE of μ_t estimate, and (2) the smallest RMSE goodness-of-fit for a VOI. We then counted across all VOIs the number of times each technique was a winner and sorted results. Based on criterion (1), we obtained the following ranking of the four best techniques: α-T-PL > PL > IT-PL > NIL-PL-TM. Based on (2), we obtained the following ranking: IL-PL-TM > α-T-PL > NIL-PL-TM > α-T-IL. Since α-T-PL was in the top two for both criteria, we deemed it best. Although IL-PL-TM had the lowest RMSE, it had a large SE uncertainty [it was not in the top four based on criterion (1)]. It is worth noting that having a smaller SE uncertainty is more significant. This is because sometimes a good numerical fit could be obtained with a high SE. Similarly, α-T-PL was voted best when we rank-ordered standard deviations across many VOIs of each tissue type. The computational complexity of α-T-PL can be greatly reduced by saving intermediate calculations.

There have been previous reports of μ_t (total attenuation coefficient) and μ_s (scattering coefficient) for atherosclerotic tissues in the literature.[29–33] Our estimates of μ_t are consistent with

Table 3 Classifier performance using optical properties features (μ_t, $\langle I \rangle$, I_0). (a) Classifier performance on 311 VOIs using α-T-PL, SVM, one-versus-rest, and fivefold cross validation. (b) VOIs with RMSE > 12 were removed, leaving 277 VOIs. Censoring improved classifier performance, particularly for lipid.

	TP	TN	FP	FN	SENSITIVITY	SPECIFICITY
(a)						
Calcium	18.4 ± 4.4	36.6 ± 5.2	4.4 ± 1.7	2.8 ± 1.9	0.86 ± 0.10	0.86 ± 0.05
Lipid	17.8 ± 4.3	40.4 ± 3.1	3 ± 1.6	1 ± 0.7	0.95 ± 0.04	0.93 ± 0.03
Fibrotic	19.6 ± 2.3	39.2 ± 4.6	0.8 ± 0.4	2.6 ± 1.7	0.89 ± 0.07	0.98 ± 0.01
(b)						
Calcium	17.4 ± 5.1	32.6 ± 5.3	2.8 ± 1.8	2.6 ± 0.9	0.86 ± 0.05	0.92 ± 0.05
Lipid	12.8 ± 2.1	40.2 ± 2.2	2 ± 1	0.4 ± 0.5	0.97 ± 0.04	$0.95 + 0.02$
Fibrotic	19.8 ± 1.8	32.2 ± 1.3	1 ± 1	2.4 ± 1.8	0.89 ± 0.08	0.97 ± 0.03

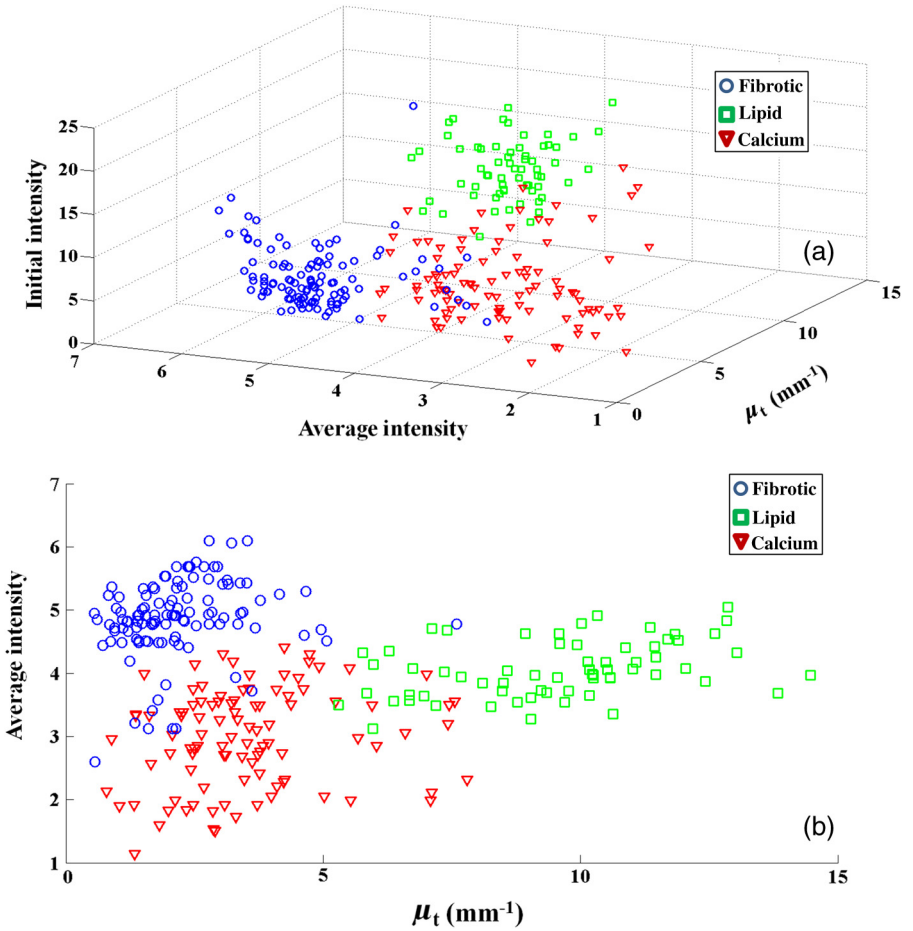

Fig. 11 (μ_t, $\langle I \rangle$, I_0) were used as features in automatic classification of VOIs using an SVM classifier into three plaque types—fibrotic, lipid, and calcium. All three features are plotted in (a) and the two best features are plotted in (b). 311 expert annotated VOIs from 35 IVOCT pullbacks. We used α-T-PL, LF, and censoring of VOIs with RMSE > 12, leaving 277. Feature space indicates a good separation between all three plaque types (calcified, fibrotic, and lipid). The (mean $\pm$ std.dev.) of μ_t estimates was: calcified (3.84 ± 0.95 mm^{-1}), fibrotic (2.15 ± 1.08 mm^{-1}), and lipid (9.99 ± 2.37 mm^{-1}). Classification results are in Table 3.

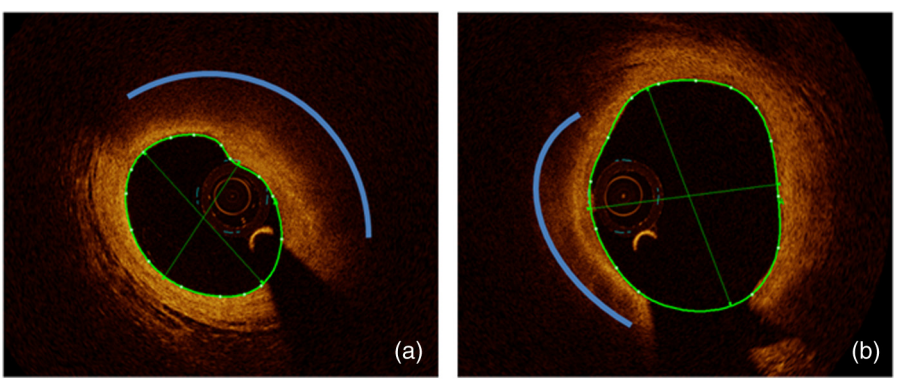

Fig. 12 Our robust estimation methods have helped us distinguish between a lipid plaque (a) and a calcified plaque with a diffuse edge (b), both shown by blue arcs. This is often a source of confusion at first glance during manual analysis. When we employed parameter estimation of μ_t, we could see a significant numerical difference between the two cases (lipid: 8.62 ± 0.66 mm^{-1}, calcium with diffuse edge: 2.06 ± 0.23 mm^{-1}), which we believe would aid in proper classification.

two previously reported studies that have estimated optical properties of clinically obtained atherosclerotic plaques using the same imaging system but different estimation procedures on stationary IVOCT acquisitions[29,30] (Table 2) [calcified (ours: 3.84 ± 0.95 mm^{-1}, reported: 2 to 5 mm^{-1}), fibrotic (ours: 2.15 ± 1.08 mm^{-1}, reported: 2 to 5 mm^{-1}), and lipid (ours: 9.99 ± 2.37 mm^{-1}, reported: $\geq$10 mm^{-1})]. Some other studies[32,33] report much lower values of μ_t for lipid (2.7 ± 0.8 mm^{-1} and 3.2 ± 1.1 mm^{-1}) and much higher values for calcified (11.1 ± 4.9 mm^{-1}), but these studies used *ex vivo* images, a bench-top OCT scanner, and a different light source, therefore, they are not comparable to our study. Another study at $\lambda_0 =$ 1300 nm[31] reported μ_s and g values instead of μ_t making comparisons difficult.

The robust, 3-D methods proposed here for measuring optical properties of tissue should be applicable to other OCT applications. Specifically, methods should be applicable to volumetric OCT cancer imaging, where optical properties have been used to distinguish cancerous tissues.[42–44]

Because it is desirable to include the quality of assessment with parameter estimates, we investigated goodness-of-fit measures. Adjusted R^2 is a good way to compare models of different orders. The PL methods (α-T-PL, PL, and IT-PL) gave higher adjusted R^2 than other methods (Fig. 10), but R^2 depends on slope and is inappropriate for assessing the fit in a particular VOI. The CV was considered, but it was determined that the CV simply favored VOIs with more A-lines. We prefer RMSE because it is simple to compute and interpret. A histogram of RMSE across many VOIs [Fig. 10(b)] shows that 90% of VOIs have "good fits" with RMSE<12. Classification results were improved when VOIs with RMSE > 12 were censored, indicating that the RMSE could be a useful feature for automated processing going forward. For example, one could estimate μ_t from regions, but additionally use the computed RMSE value as a confidence in the μ_t estimate and weight the feature accordingly during classification.

The exploratory classification study yielded surprisingly good results based solely on optical property parameters (Table 3, Fig. 11). The choice of classifier and other parameter settings was determined from preliminary optimization experiments in which a small subset of VOIs of all three plaque types was employed. We used SVM, three tissue types, one-against-all training, three features (μ_t, $\langle I \rangle$, I_0), and fivefold cross validation to assess results. Censoring VOI data with poor fits (RMSE > 12) improved sensitivity and specificity as compared with uncensored data for calcium and lipid VOIs, and only slightly lowered specificity (while keeping the same sensitivity) for fibrotic VOIs [Tables 3(a) versus 3(b)]. It was encouraging that the optical parameter estimates allowed us to distinguish between lipid plaques and calcium plaques with a diffuse edge, often a problem during manual analysis (Fig. 12). In manual analysis, analysts typically analyze adjacent 2-D frames to make a determination using standard definitions provided by Yabushita et al.[13] It is promising that the computational methods can determine this from optical properties alone.

The aim of our study was to compare advanced parameter estimation methods applicable to clinical 3-D IVOCT pullbacks. This avoids the use of *ex vivo* data with its potential limitations including potential tissue degradation, no mean or pulsating pressure, no cardiac motion, unrealistic temperatures, no blood artifacts, and a straight path pullback rather than actual 3-D coronary geometry. Moreover, in the event of spatially inaccurate, sparse histological sampling, one can make inappropriate "ground truth" determinations using *ex vivo* data. Instead we used as ground truth VOIs identified by well-trained analysts using well-established criteria. Our VOI classification results overestimate that which would be obtained in automatic processing of pullback data. That is, analysts choose homogeneous, easily identified VOIs, giving rise to relatively unambiguous computer classification. In addition, analysts purposely did not choose regions of macrophages and thrombi because we were focusing on optical attenuation estimation rather than other features. Our approach should be quite appropriate for optimizing the 3-D parameter estimation methods in this report.

In summary, we believe that the robust processing methods make it possible to assess tissue optical properties from noisy, IVOCT clinical pullback data. In addition, optical parameters thus obtained will be important image features for an automated analysis of plaques. We believe that the 3-D methods reported here for assessing optical properties will also be applicable in volumetric OCT cancer imaging.

Acknowledgments

This project was supported by the National Heart, Lung, and Blood Institute through Grants NIH R21HL108263 and 1R01HL114406-01 and by the National Center for Research Resources and the National Center for Advancing Translational Sciences through Grant UL1RR024989. These grants are a collaboration between Case Western Reserve University and University Hospitals of Cleveland.

References

1. I. K. Jang et al., "*In vivo* characterization of coronary atherosclerotic plaque by use of optical coherence tomography," *Circulation* **111**, 1551–1555 (2005).
2. T. Kume et al., "Assessment of coronary arterial plaque by optical coherence tomography," *Am. J. Cardiol.* **97**, 1172–1175 (2006).
3. F. Prati et al., "Expert review document on methodology, terminology, and clinical applications of optical coherence tomography: physical principles, methodology of image acquisition, and clinical application for assessment of coronary arteries and atherosclerosis," *Eur. Heart J.* **31**, 401–415 (2010).
4. R. Puri, M. I. Worthley, and S. J. Nicholls, "Intravascular imaging of vulnerable coronary plaque: current and future concepts," *Nat. Rev. Cardiol.* **8**, 131–139 (2011).
5. D. Stamper, N. J. Weissman, and M. Brezinski, "Plaque characterization with optical coherence tomography," *J. Am. Coll. Cardiol.* **47**, C69–C79 (2006).
6. W. M. Suh et al., "Intravascular detection of the vulnerable plaque," *Circ.: Cardiovasc. Imaging* **4** (2), 169–178 (2011).
7. M. J. Suter et al., "Progress in intracoronary optical coherence tomography," *IEEE J. Sel. Top. Quantum Electron.* **16**, 706–714 (2010).
8. G. J. Tearney, I. K. Jang, and B. E. Bouma, "Imaging coronary atherosclerosis and vulnerable plaques with optical coherence tomography," in *Optical Coherence Tomography*, pp. 1083–1101, Springer, Berlin, Heidelberg (2008).
9. G. J. Tearney et al., "Quantification of macrophage content in atherosclerotic plaques by optical coherence tomography," *Circulation* **107**, 113–119 (2003).
10. G. J. Tearney, I. K. Jang, and B. E. Bouma, "Optical coherence tomography for imaging the vulnerable plaque," *J. Biomed. Opt.* **11**, 021002 (2006).
11. S. Tahara et al., "Intravascular optical coherence tomography detection of atherosclerosis and inflammation in murine aorta," *Arterioscler., Thromb., Vasc. Biol.* **32**, 1150–1157 (2012).
12. H. G. Bezerra et al., "Intracoronary optical coherence tomography: a comprehensive review, clinical and research applications," *JACC: Cardiovasc. Interventions* **2**, 1035–1046 (2009).

13. H. Yabushita et al., "Characterization of human atherosclerosis by optical coherence tomography," *Circulation* **106**, 1640–1645 (2002).
14. I. K. Jang et al., "Visualization of coronary atherosclerotic plaques in patients using optical coherence tomography: comparison with intravascular ultrasound," *J. Am. Coll. Cardiol.* **39**, 604–609 (2002).
15. Z. Wang et al., "Semiautomatic segmentation and quantification of calcified plaques in intracoronary optical coherence tomography images," *J. Biomed. Opt.* **15**, 061711 (2010).
16. Z. Wang et al., "Automatic segmentation of intravascular optical coherence tomography images for facilitating quantitative diagnosis of atherosclerosis," *Proc. SPIE* **7889**, 78890N (2011).
17. Z. Wang et al., "Volumetric quantification of fibrous caps using intravascular optical coherence tomography," *Biomed. Opt. Express* **3**, 1413 (2012).
18. Z. Wang et al., "Single-shot stent segmentation in intravascular OCT pullbacks," in *Biomedical Optics*, p. BTu4B-5, Optical Society of America (2012).
19. H. Lu et al., "Automatic stent strut detection in intravascular OCT images using image processing and classification technique," *Proc. SPIE* **8670**, 867015 (2013).
20. H. Lu et al., "Automatic stent detection in intravascular OCT images using bagged decision trees," *Biomed. Opt. Express* **3**, 2809–2824 (2012).
21. S. Tahara et al., "Angiographic, IVUS and OCT evaluation of the long-term impact of coronary disease severity at the site of overlapping drug-eluting and bare metal stents: a substudy of the ODESSA trial," *Heart* **96**, 1574–1578 (2010).
22. H. Kyono et al., "Optical coherence tomography (OCT) strut-level analysis of drug-eluting stents (DES) in human coronary bifurcations," *EuroIntervention* **6**, 69–77 (2010).
23. G. Guagliumi et al., "Strut coverage and vessel wall response to a new-generation paclitaxel-eluting stent with an ultrathin biodegradable abluminal polymer: Optical Coherence Tomography Drug-Eluting Stent Investigation (OCTDESI)," *Circ. Cardiovasc. Intervention* **3**(4), 367–375 (2010).
24. G. Guagliumi et al., "Optical coherence tomography assessment of in vivo vascular response after implantation of overlapping bare-metal and drug-eluting stents," *JACC: Cardiovasc. Interventions* **3**, 531–539 (2010).
25. S. J. Kang et al., "Optical coherence tomographic analysis of in-stent neoatherosclerosis after drug-eluting stent implantation," *Circulation* **123**, 2954–2963 (2011).
26. A. Knu, S. Bonev, and W. Knaak, "New method for evaluation of *in vivo* scattering and refractive index properties obtained with optical coherence tomography," *J. Biomed. Opt.* **9**, 265–273 (2004).
27. O. Manfrini et al., "Sources of error and interpretation of plaque morphology by optical coherence tomography," *Am. J. Cardiol.* **98**, 156–159 (2006).
28. G. van Soest et al., "Pitfalls in plaque characterization by OCT image artifacts in native coronary arteries," *JACC Cardiovasc. Imaging* **4**, 810–813 (2011).
29. C. Xu et al., "Characterization of atherosclerosis plaques by measuring both backscattering and attenuation coefficients in optical coherence tomography," *J. Biomed. Opt.* **13**, 034003 (2008).
30. G. van Soest et al., "Atherosclerotic tissue characterization *in vivo* by optical coherence tomography attenuation imaging," *J. Biomed. Opt.* **15**, 011105 (2010).
31. D. Levitz et al., "Determination of optical scattering properties of highly-scattering media in optical coherence tomography images," *Opt. Express* **12**, 249–259 (2004).
32. D. J. Faber et al., "Quantitative measurement of attenuation coefficients of weakly scattering media using optical coherence tomography," *Opt. Express* **12**, 4353–4365 (2004).
33. F. J. Van der Meer et al., "Localized measurement of optical attenuation coefficients of atherosclerotic plaque constituents by quantitative optical coherence tomography," *IEEE Trans. Med. Imaging* **24**, 1369–1376 (2005).
34. G. van Soest et al., "Frequency domain multiplexing for speckle reduction in optical coherence tomography," *J. Biomed. Opt.* **17**, 076018 (2012).
35. Y. Yang et al., "Optical scattering coefficient estimated by optical coherence tomography correlates with collagen content in ovarian tissue," *J. Biomed. Opt.* **16**, 090504 (2011).
36. P. Lee, W. Gao, and X. Zhang, "Performance of single-scattering model versus multiple-scattering model in the determination of optical properties of biological tissue with optical coherence tomography," *Appl. Opt.* **49**, 3538–3544 (2010).
37. L. S. Athanasiou et al., "Methodology for fully automated segmentation and plaque characterization in intracoronary optical coherence tomography images," *J. Biomed. Opt.* **19**, 026009 (2014).
38. G. J. Ughi et al., "Automated tissue characterization of in vivo atherosclerotic plaques by intravascular optical coherence tomography images," *Biomed. Opt. Express* **4**, 1014–1030 (2013).
39. J. S. Lee, "Speckle analysis and smoothing of synthetic aperture radar images," *Comput. Graphics Image Process.* **17**, 24–32 (1981).
40. H. Theil, *Economic Forecasts and Policy*, North-Holland Publication (1961).
41. Y. Tang et al., "SVMs modeling for highly imbalanced classification," *IEEE Trans. Syst., Man, Cybern. B* **39**, 281–288 (2009).
42. S. Wang et al., "Three-dimensional computational analysis of optical coherence tomography images for the detection of soft tissue sarcomas," *J. Biomed. Opt.* **19**(2), 021102 (2014).
43. L. Scolaro et al., "Parametric imaging of the local attenuation coefficient in human axillary lymph nodes assessed using optical coherence tomography," *Biomed. Opt. Express* **3**(2), 366–379 (2012).
44. P. Robbins et al., "Parametric imaging of cancer with optical coherence tomography," *J. Biomed. Opt.* **15**(4), 046029 (2010).

Madhusudhana Gargesha is a senior research associate in the Department of Biomedical Engineering at Case Western Reserve University, Cleveland, Ohio, USA. He received his BE degree in electronics and communication engineering from Bangalore University, Bangalore, India, in 1997, and his MS and PhD degrees in electrical engineering from Arizona State University, Tempe, Arizona, in 2002 and 2006, respectively. He is the author of more than 15 journal papers and 20 conference publications. His current research interests include 3-D image analysis, processing, and visualization as applied to medical and biological imaging modalities including IVOCT, MRI, and block-face cryo-imaging.

Ronny Shalev spent much of the past 21 years in executive positions in public and private companies. Currently, he is an advanced PhD student having extraordinary product development experience. He holds an MSc in electrical engineering and applied physics. His current research interests include medical image processing, machine learning, and visualization as applied to various medical and biological imaging modalities.

David Prabhu is a senior level PhD candidate at Case Western Reserve University. He is a Choose Ohio First Scholar and has industrial experience in the field of cryo-imaging. His research interests include image processing and analysis, 3-D visualization, histology, and cryo-imaging.

Kentaro Tanaka is the research fellow of the Cardiovascular Imaging Core Laboratory, Harrington Heart and Vascular Institute, University Hospitals Case Medical Center. His interests are cardiovascular imaging, coronary artery OCT, and IVUS.

Andrew M. Rollins is a professor of biomedical engineering and medicine at Case Western Reserve University. His research interests are in the development and application of advanced optical technologies, especially optical coherence tomography and optical stimulation, to the study of developmental biology and to endoscopic imaging of cardiovascular disease and cancer. He directs an NIH-funded research program and has trained numerous MS and PhD students.

Marco Costa is a professor of medicine, CWRU, Angela & James Hambrick Master Clinician in Innovation, board-certified interventional cardiologist, director of the Interventional Cardiovascular Center, and director of the Research and Innovation Center University Hospitals, Case Medical Center. He has been a leader in developing IVOCT as well as new interventional procedures. He was the first person in the US to perform clinical OCT imaging with an FDA-approved OCT imaging system from LightLab, now St. Jude.

Hiram G. Bezerra is an assistant professor of medicine, CWRU, board-certified interventional cardiologist, and medical director of the Cardiovascular Imaging Core Laboratory at University Hospitals (Core Lab), Case Medical Center. Under his Core Lab duties, he is responsible for the analysis of thousands of cardiovascular images from IVOCT as well as other modalities, e.g., intravascular ultrasound, quantitative angiography, cardiac MRI, and cardiac CT. He directs both state and federal research grants.

David L. Wilson is the Robert Herbold professor of biomedical engineering and radiology, Case Western Reserve University. His interests are image processing and analysis, cardiovascular imaging, coronary artery OCT, and cryo-imaging. He serves on NIH study sections, editorial boards, and conference committees. He has trained numerous PhD students and postdocs, all of whom are quite exceptional. In addition to federal and state funded research activities, he is the director of CWRU's Interdisciplinary Biomedical Imaging NIH T32 training grant.